Journal of Materials Chemistry C

Accepted Manuscript

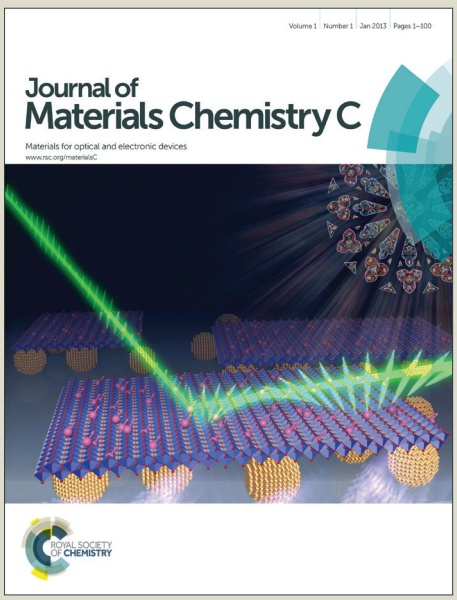

ROYAL SOCIETY OF CHEMISTRY

www.rsc.org/materialsC

Journal of Materials Chemistry C RSCPublishing

ARTICLE

Diketopyrrolopyrrole (DPP) Functionalized Tetrathienothiophene (TTA) Small Molecules for Organic Thin Film Transistors and Photovoltaic Cells

Cite this: DOI: 10.1039/x0xx00000x

Received 00th January 2014,
Accepted 00th January 2014

DOI: 10.1039/x0xx00000x

www.rsc.org/

Nanjia Zhou,[a‡] Sureshraju Vegiraju,[b‡] Xinge Yu,[c] Eric F. Manley,[c] Melanie R. Butler,[c] Matthew J. Leonardi,[c] Peijun Guo,[a] Wei Zhao,[d] Yan Hu,[d] Kumaresan Prabakaran,[b] Robert P. H. Chang,[a] Mark A. Ratner,[c] Lin X. Chen,[c] Antonio Facchetti,[c,d]* Ming-Chou Chen,[b]* Tobin J. Marks,[a,c]*

Two novel π-conjugated small molecules based on the electron-deficient diketopyrrolopyrrole (DPP) and the electron-rich fused tetrathienoacene (TTA) frameworks are synthesized and characterized. As verified in the bandgap compression of these chromophores by electrochemistry and density functional theory (DFT) computation, these DPP-TAA derivatives exhibit substantial conjugation and ideal MO energetics for light absorption. The large fused TTA core and strong intermolecular S···S interactions enforce excellent molecular planarity, favoring a close-packed thin film morphologies for efficient charge transport, as indicated by grazing incidence wide angle X-ray scattering (GIWAXS), atomic force microscopy (AFM), and transmission electron microscopy (TEM) analysis. Top-gate/bottom-contact thin film transistors based on these systems exhibit hole mobilities approaching 0.1 $cm^2V^{-1}s^{-1}$. Organic photovoltaic cells based on DDPP-TTAR:$PC_{71}BM$ blends achieve power conversion efficiencies (PCE) > 4% by systematic morphology tuning and judicious solvent additive selection.

Introduction

Organic semiconductors are suitable candidates for the high-throughput, large-scale, inexpensive, and environmentally benign manufacture of diverse opto-electronic devices. Over the past two decades, a number of polymeric and small molecule materials have been successfully employed in both organic thin film transistors (OTFTs) and organic solar cells (OSCs), two of the most investigated semiconductor device classes.[1-5] Toward the goal of better understanding and commercializing these new materials technologies, the development of novel organic semiconductors has been a major driver for enhancing device performance, and remains at the forefront of current R&D.

For the design of small molecule semiconductors, a donor-acceptor (D-A) strategy is commonly employed to specifically tune the highest occupied molecular orbital (HOMO) and lowest unoccupied molecular orbital (LUMO) energies for broader solar light absorption, for ohmic contact at electrode interfaces, and to maximize built-in OSC potentials. Among various conjugated building blocks, the electron-deficient diketopyrrolopyrrole (**DPP**) moiety has received extensive attention due to its tunable solubility and relatively high electron affinity for adjusting orbital energetics.[6-15] By installing proper alkyl side chains at the **DPP** nitrogen atoms, the processability of the resulting **DPP** derivatives can be enhanced, rendering them compatible with roll-to-roll solution processing.[16] The most noteworthy examples of **DPP**-based polymers have high hole mobilities, up to 12-13.9 $cm^2V^{-1}s^{-1}$ in OTFTs.[17, 18] (structures shown in Scheme 1A), and DPP based polymers combined with fused thiophenes such as thienothiophene (**TT**) and dithienothiophene (**DTT**) as donor units have p-type charge-carrier mobilities as high as 10.5 $cm^2V^{-1}s^{-1}$ [19]. and power conversion efficiencies up to 6.05-9.4% in OSCs[20, 21] (structure shown in Scheme 1B and 1C).

Despite the success of the aforementioned **DPP**-based polymers, the development and understanding of **DPP**-based small molecules has lagged far behind. Unlike polymer syntheses and properties, which are

typically susceptible to batch-to-batch variations, small molecule syntheses generally provide excellent reproducibility, purity, and yields, leading for far more uniform materials properties.[3, 22-25] For these

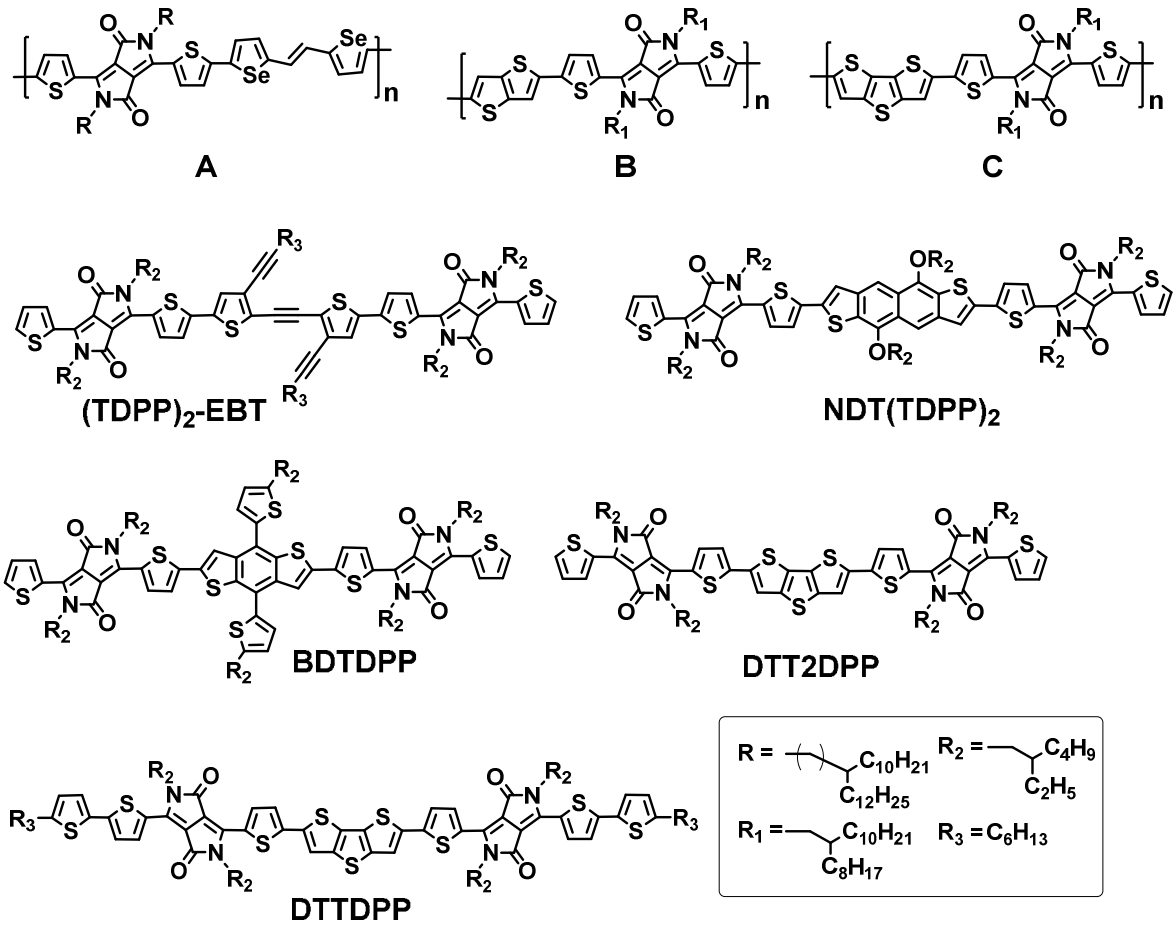

Scheme 1. Examples of DDP-fused thiophene organic semiconductors.

reasons, solution-processable small molecules offer great potential for applications in technologically relevant organic electronic devices. Furthermore, small molecules can achieve precisely controlled molecular packing and ordered nanophase morphologies, via either self-assembly or controlled solution coating techniques.[26, 27] Thus, the design and implementation of small molecules also opens new possibilities for understanding fundamental organic semiconductor structure-property relationships and further optimizing device parameters. Nevertheless, to date only relatively low p-type mobilities and PCEs have been achieved using **DPP**-based small molecules.[10] For example, our team first reported **NDT(TDPP)$_2$** (Scheme 1) exhibiting OPV PCEs of up to 4%,[28] followed by alkyne functionalized

$(TDPP)_2$-EBT exhibiting a mobility of 0.17 $cm^2V^{-1}s^{-1}$ and a PCE of 1.7%.[29] More recently, Huang et. al.[30] and Lin et al.[14] combined **DPP** with the widely implemented benzodithiophene (**BDT**) moiety and demonstrated OSC PCEs of >5%. While these results are promising, more detailed investigations will be necessary to better understand and further enhance the TFT and OPV device performance of **DPP**-based small molecules.

Motivated by the potential of introducing fused thiophene units into electronic polymers, here we investigate fused thiophenes systems for the design of high performance small molecule materials. From our previous results, fused thiophene motifs enhance structural planarity and strong intermolecular S···S interactions.[31-33] These properties promote extensive intramolecular π-conjugation and close intermolecular π-π stacking, thereby enhancing charge transport.[34, 35] Indeed, dithienothiophene-(**DTT**)[36-39] and tetrathienoacene-(**TTA**)[35] derivatives achieve field-effect mobilities as high as 10.2 and 0.30 $cm^2V^{-1}s^{-1}$ for p- and n- channel OTFTs, respectively. However, on combining fused thiophenes with **DPP** units, **DPP**-end-capped **DTT** (**DTT2DPP**) and **DTTDPP** derivatives yield only modest OTFT mobilities of ~0.02 $cm^2V^{-1}s^{-1}$,[40] and OSC PCEs approaching ~2.2%[41]. To enhance device performance based on this design principle, we now integrate an additionally conjugated fused thiophene, **TTA** (Scheme 1), with **DPPs** as acceptor moieties. Such acene-based chromophores are expected to have more expansive planarity for π-π stacking and enhanced charge transport characteristics which are crucial for OTFT and OSC performance.

In this contribution we report two new semiconductors based on a β-alkyl substituted **TTA** core[42] end-capped with two **DPP** moieties: N-alkylated **DPPs** and O-alkylated **DPPs**[43] (referred to as **DPP'** herein). Note that **DPP'** derivatives are known to have smaller energy gaps and lower-lying HOMO energies than the **DPP** analogues.[43] These characteristics are beneficial for both OTFT and OSC devices. However to date no **DPP'**-based small molecules have been explored for applications in organic electronics and are thus investigated here for comparison. Solution-processed OTFT and OSC devices are

fabricated here based with these two molecules, and exhibit PCEs of up to 4% and hole mobilities approaching 0.1 $cm^2V^{-1}s^{-1}$, rendering these the highest performing fused thiophene OSC chromophores and some of the highest mobility fused thiophene semiconductors reported to date.

Results and Discussion

1. Synthesis

A generalizable synthetic approach to molecules **1** and **2** is presented in Schemes 2 and 3. **DPP** functionalized TTAs (**1**) and (**2**) are synthesized via Stille coupling, as shown in Scheme 2. Alkylated tetrathienothiophene (**TTAR**; **3**), prepared according to literature procedures,[42] is first di-deprotonated with *n*-BuLi, and then di-alkylstannylated to generate distannyl tetrathienothiophene (**4**), which can be recrystallized from ether and obtained in 67% yield. The mono-brominated N-alkyl and the O-alkyl DPP-based aryl bromides **5**[28] and **6**[43] are prepared in ~50% yields according to previously published procedures (Scheme 3). These units are then coupled with **4** to give the **DPP** end-capped **DDPP-TTAR** (**1**) and **DDPP'-TTAR** (**2**) in ~ 66% and 62% yield, respectively. The new molecules were then purified by chromatography and recrystallization from CH_2Cl_2 to give materials suitable for used in OTFT and OSC devices. To the best of our knowledge this newly synthesized **DDPP'** acceptor moiety is employed

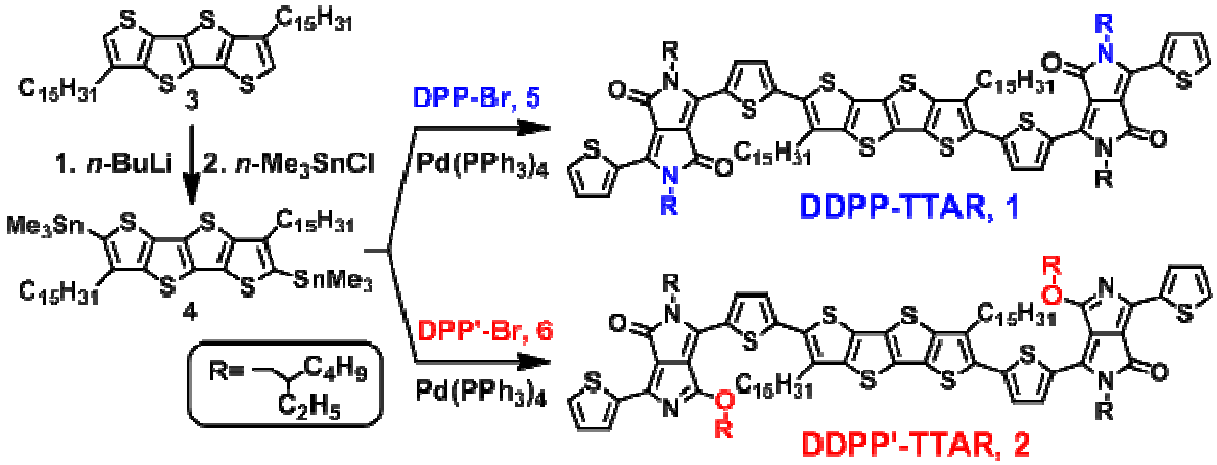

Scheme 2. Synthesis of semiconductors DDPP-TTAR (**1**) and DDPP'-TTAR (**2**).

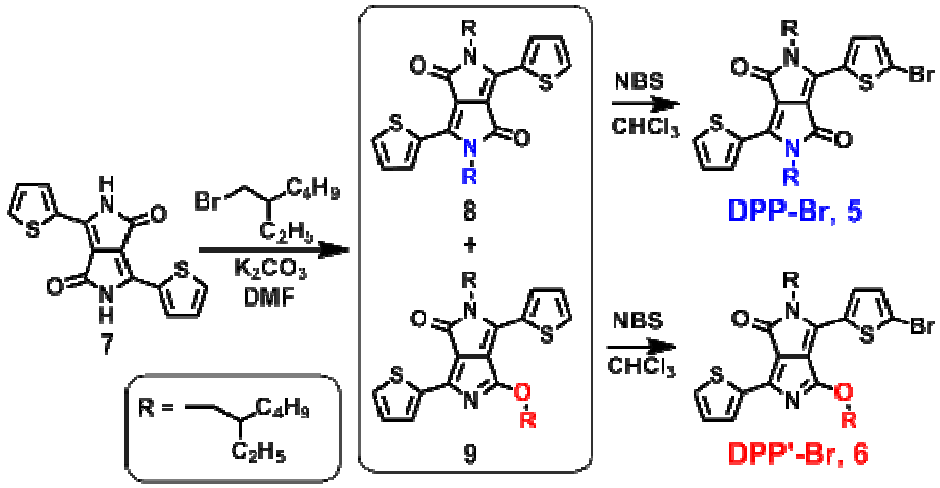

Scheme 3. Synthesis of semiconductors DPP-Br (**5**) and DPP'-Br (**6**).

for the first time in small molecules for organic electronics objectives. All new compounds are characterized by conventional chemical and physical methodologies. Full experimental details can be found in the ESI.

2. Thermal, Optical, and Electrochemical Properties of DDPP-TTARs (1 and 2)

For the new molecular semiconductors **1** and **2**, differential scanning calorimetry (DSC) data reveal sharp endotherms at 222°C and 128°C, respectively, while thermogravimetric analysis (TGA) plots demonstrate negligible weight loss (~5%) until ca. 375°C and 294°C, respectively, as summarized in Table 1. Thus, under the same conditions, a higher melting point as well as greater thermal stability is observed for **1** versus isomer **2**.

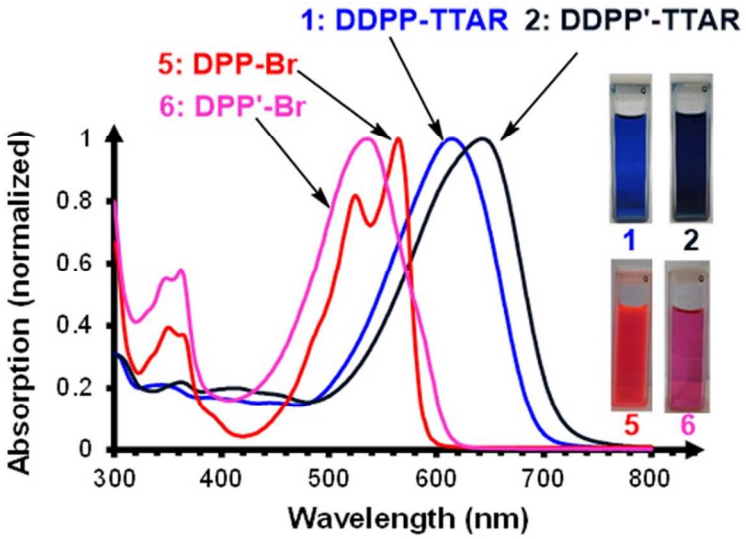

Figure 1. Optical spectra of mono-brominated **DPPs** and **DDPP-TTAR** (**1**) and **DDPP'-TTAR** (**2**) in o-$C_6H_4Cl_2$ solution.

Molecules **1** and **2** both show visible light absorption over a broad range, making them excellent candidates for OSCs. The optical absorption spectrum of **2** in *o*-$C_6H_4Cl_2$ (Figure 1) is significantly red-shifted versus that of **1** ($E_{opt,\ gap}$ = 1.69 eV), indicating greater π-electron delocalization and a compressed optical band gap ($E_{opt,\ gap}$ = 1.66 eV; Table 1), in good agreement with the band gap values obtained from electrochemical measurements (*via infra*). The stability of these two compounds with respect to photooxidation was also investigated by monitoring the decay of the optical absorption maxima in aerated *o*-$C_6H_4Cl_2$ solutions exposed to a white fluorescent lamp light at room temperature. No decomposition is observed after several days of continuous illumination.

Differential pulse voltammograms (DPVs; see Figure S1) of **1** and **2** were next recorded in *o*-$C_6H_4Cl_2$ at 25 ^{o}C, and data are summarized in Table 1. The DPV of **1** exhibits an oxidation peak at +0.92 V and a reduction peak at -1.02 V, whereas those of **2** are located at lower potentials (E_{ox} = +0.86 V and E_{red} = -0.91 V). The estimated HOMO (-5.12 eV) and LUMO (-3.17 eV) of **1** thus lie below than those of **2** (-5.06 eV and -3.28 eV, Figure 2b, Table 1), corresponding to a smaller band gap for the latter. HOMO energies (EHOMO) were estimated using the conventional equation, E_{HOMO} = -(4.20 + E_{ox}); assuming ferrocene/ferrocenium oxidation at -4.8 eV. The low-lying HOMO energies for the two **DDPP-TTARs**

suggest that the two molecules should have good air stability versus pentacene and other previously reported fused thiophenes employing **DTTs** or **TTAs**.[28,30] Furthermore, the HOMO energies of the present **TTA** compounds have ideal alignment favoring hole injection from contacting Ag electrodes in p-type TFTs.

Table 1. Thermal, optical, and electrochemical properties of semiconductors **1** and **2**.

Cmpd.	DSC T_m (°C)	TGA (°C; 5%)	UV-Vis λ_{max} (nm) [a]	E_{red} (V) [b]	LUMO (eV)	E_{ox} (V)[b]	HOMO (eV)	ΔE_{gap} (eV)	
								UV [d]	DPV [b]
1	222	375	615	-1.02	-3.17[c]	0.92	-5.12[c]	1.69	1.95
2	128	294	643	-0.91	-3.28[c]	0.86	-5.06[c]	1.66	1.77

[a] In *o*-$C_6H_4Cl_2$. [b] by DPV in *o*-$C_6H_4Cl_2$ at 25 °C. All potentials referenced to an Fc^+/Fc internal standard (at +0.6 V). E_{red} = reductive potential; E_{ox} = oxidative potential. [c] Using HOMO= -(4.2+ E_{ox}); LUMO= -(4.2+ E_{red}). [d] Energy gap estimated from optical absorption.

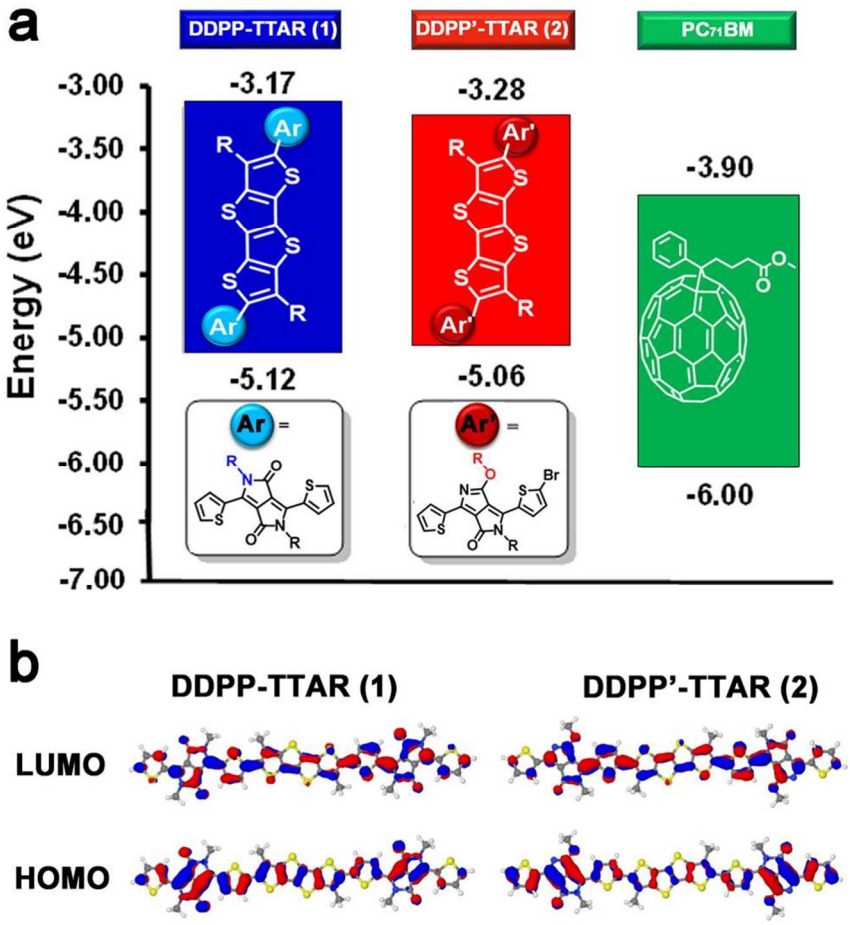

Figure 2. Energetic alignment of molecules **1** and **2**. a) DPV-derived HOMO and LUMO energy levels; b) DFT-derived molecular orbital contours.

Electronic structure calculations were performed at the B3LYP/6-31G** level of density functional theory (DFT; Figure 2b). Both molecules have similar ground state geometries characterized by relatively coplanar backbones, with the HOMO level electron density clearly localized on the **DPP** donor and the **TTA** moieties. The computed HOMO energies are -4.79 eV and -4.90 eV for **1** and **2**, respectively, and the excited state (LUMO) energies for **1** and **2** are -2.80 eV and -2.99 eV, respectively, yielding optical gaps of 1.99 and 1.91 eV for **1** and **2**, respectively. That **2** has lower computed HOMO/LUMO energies as well as a compressed band gap versus **1**, agrees well with the experimental

optical absorption and DPV data.[43] Time-dependent DFT (TDDFT) computations show that the principal optical transitions of **1** and **2** exhibit similar oscillator strengths, (2.67 and 2.64, respectively), in good agreement with the experimental extinction coefficients for **1** and **2** (82,900 and 125,000 $M^{-1}cm^{-1}$, respectively).

3. Film morphology and charge transport properties

Grazing incidence X-ray diffraction (GIXRD) and AFM were employed to characterize the film morphologies of the two **TTAR** materials, and were performed on thin films prepared by spin-coating chloroform (CF) solutions of **1** and **2** onto Si/SiO_2 substrates (Figure 3). Furthermore, to identify the effects of post-annealing on molecular ordering, which can provide guidelines for OTFT fabrication, GIXRD and AFM data were also collected on films processed at various post-annealing temperatures. The pristine films fabricated at room temperature show relatively modest crystallinity for both **1** and **2** (Figures 3a, b). The

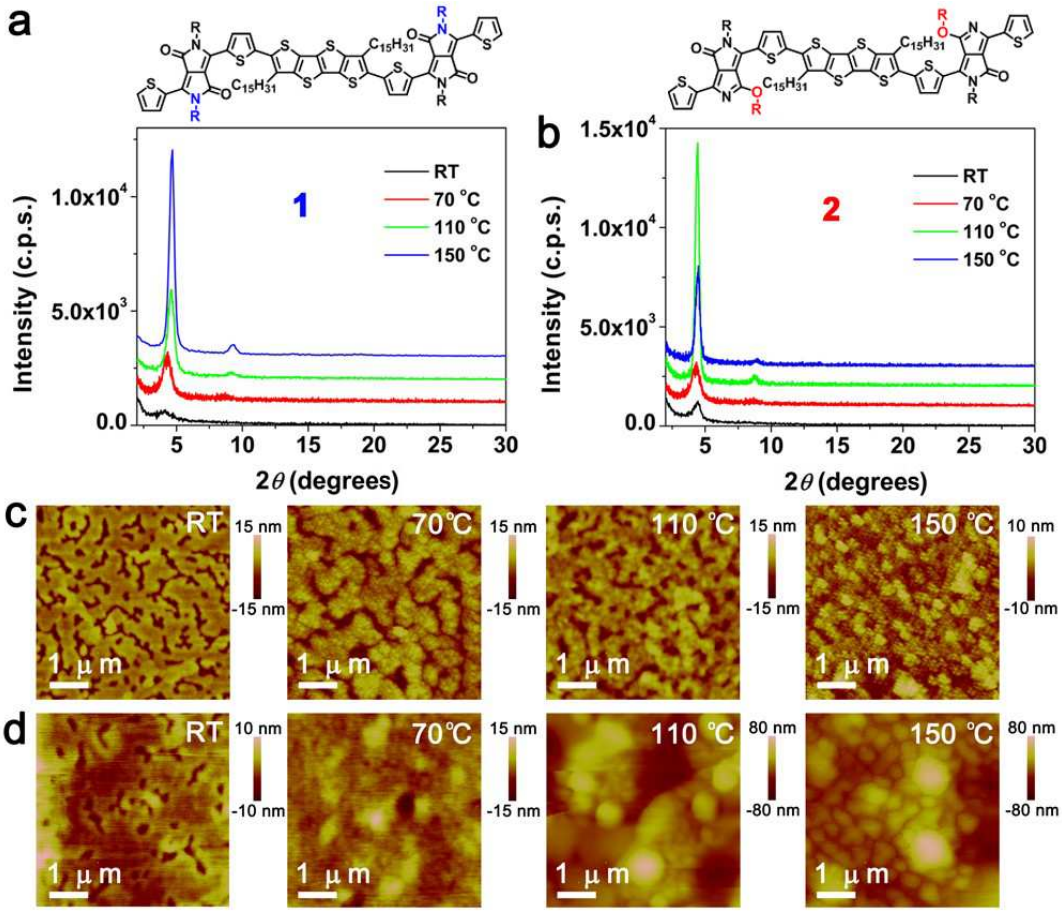

Figure 3. Film morphology for semiconductors **1** and **2** as a function of post-deposition thermal annealing. a, b) GIXRD and c ,d) AFM topographical images of **1** and **2** after annealing at the indicated temperatures.

The first-order diffraction peaks (100) are located at 2θ = 4.2˚ and 4.5˚, corresponding to d-spacings of 21.0 and 19.6 Å, for **1** and **2**, respectively. However, film crystallinity for both molecules is dramatically enhanced upon thermal annealing. For **1**, the GIXRD patterns exhibit increasing intensities of the (100) diffraction peaks with increasing annealing temperatures, showing second-order reflections for films annealed above 110 ˚C (at 2θ = 9.3˚). Enhanced crystallinity on annealing can also be inferred from the AFM images (Figure 3c). Interestingly for **2**, the crystallinity gradually increases with increasing temperature up to ~110 ˚C, but then falls for temperatures above 150 ˚C. This result agrees well with the AFM topographical images, with the film annealed at 150 ˚C exhibiting significantly smaller grains than those annealed at 110 ˚C.

To investigate the charge transport properties of **1** and **2**, bottom-gate top-contact (BGTC) OTFTs were first fabricated using heavily n-doped Si as the gate, 300 nm SiO_2 as the dielectric, and spin-coated organic semiconductor layers. The films were examined at room temperature after annealing at 70, 110, or 150 ˚C. Finally, gold (Au) source/drain (s/d) electrodes with a channel width/length of 1000/50 μm were evaporated on top of the organic layer, and the completed TFTs were characterized in ambient air (Figure 4). All devices show p-type transistor behavior and no ambipolar characteristics, with the relevant FET metrics summarized in Table 2. The TFTs based on the unannealed **1** films yield an average hole mobility (μ_h) of 3.8×10^{-4} $cm^2V^{-1}s^{-1}$, ~2.4x greater than those of molecule **2**. With thermal annealing at various temperatures, the μ_h of **1** is found to significantly increase to 7.7×10^{-4} $cm^2V^{-1}s^{-1}$at 70 ˚C, and further reach 1.2×10^{-2} $cm^2V^{-1}s^{-1}$ for annealing at 110 ˚C. However, annealing **1** films at higher temperatures decreases the hole mobility, with 4.5×10^{-3} $cm^2V^{-1}s^{-1}$ measured for 150 ˚C annealing. In contrast, the TFT performance of semiconductor **2** decreases upon post-deposition thermal annealing, which is likely the result of grain boundary formation. These transport results are consistent with the AFM images shown in Figure 3d, where higher annealing temperatures result in small "island" formation, thus compromising the connectivity required for efficient charge transport.

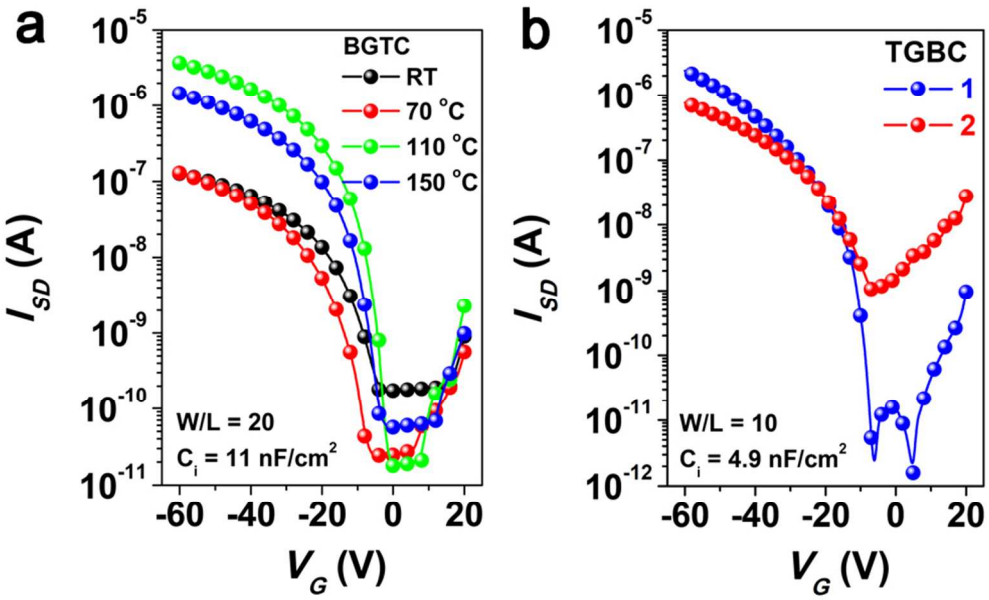

Figure 4. OTFT characteristics of semiconductors **1** and **2**. a) Transfer plots of **1** unannealed **1** films yield an average hole mobility (μ_h) of 3.8×10^{-4} $cm^2V^{-1}s^{-1}$, ~2.4 times greater than that of semiconductor **2**. With thermal annealing at various temperatures, the μ_h of **1** is found to substantially increase to 7.7×10^{-4} $cm^2V^{-1}s^{-1}$at 70 ˚C, and increase to 1.2×10^{-2} $cm^2V^{-1}s^{-1}$ at 110 ˚C; b) Transfer plots of **1** and **2** in TGBC device configurations, after annealing at 110 ˚C.

Table 2. TFT performance metrics (hole/electron mobilities, I_{on}/I_{off} ratios, and threshold voltages, V_t) for small molecule films in bottom-gate/top-contact (BGTC) devices upon post-deposition annealing at the indicated temperatures. Average values for five devices are shown.

Semi-conductor	Annealing temperature (˚C)	μ_h ($cm^2V^{-1}s^{-1}$)	On/off	V_t (V)
1	RT	3.8×10^{-4}	10^3	-9.5
	70	7.7×10^{-4}	10^4	-18
	110	1.2×10^{-2}	10^5	-4.9
	110 (BCTG)*	9.1×10^{-2}	10^5	-26.4
	150	4.5×10^{-3}	10^4	-8.7
2	RT	1.4×10^{-3}	10^3	-11.2
	70	6.4×10^{-4}	10^3	-9.7
	110	1.7×10^{-4}	10^3	-6.4
	110 (BCTG)*	1.8×10^{-2}	10^3	-15.6
	150	5.3×10^{-5}	10^2	-10.5

*Bottom contact, top gate device geometry

Next, the top-gate/bottom-contact (TGBC) TFT architectures were adopted to further enhance the OTFT performance. Thus, Si/SiO_2 wafers with patterned Au s/d electrodes were utilized as substrates, and both **1** and **2** solutions were spin-coated on these and post-annealed at various temperatures. Subsequently, a Cytop layer with a unit capacitance of 4.9 nF/cm^2 was spun-cast as the top gate dielectric layer.[44] Finally, Au contacts were evaporated onto the dielectric as the gate electrodes. Here, optimum results are achieved by measuring **1** and **2** in vacuum and after annealing at 110 °C. TFTs based on

semiconductor **1** yield a hole mobility of ~ 0.1 $cm^2V^{-1}s^{-1}$, whereas those base on **2** yield a μ_h value up to ~2×10^{-2} $cm^2V^{-1}s^{-1}$. Clearly Cytop improves device characteristics, likely via reduction of the interfacial traps arising from the suboptimal film morphology, particularly for semiconductor **2**. Despite having favorable energetics, the fact that semiconductor **2** exhibits overall lower TFT performance can be explained by a combination of relatively poor intermolecular packing and macroscopically suboptimal morphology (Figure 3).

4. Bulk-Heterojunction Film Properties and OSC Fabrication

It is well-known that the nanophase morphology of bulk-heterojunction OSC donor-acceptor blends can be strongly affected by the processing conditions.[22, 45, 46] Straightforward out-of-plane GIXRD can provide insightful information regarding molecular crystallinity and packing, thus directly yielding guidelines for the fabrication conditions to be used for OSCs. Specifically, here we investigate the effects of 1,8-diiodooctane (DIO) as a solvent additive, which can play a significant role in modifying the crystallinity of small molecule blends and D-A phase separation.[32, 47] To identify the effects of DIO on the molecular packing of the new semiconductors, GIXRD measurements were first performed on neat films of **1** and **2**, spin-cast from chloroform (CF) solutions with varying amounts of DIO as the processing additive. The GIXRD measurements (Figure 5) indicate that DIO addition introduces a higher degree of ordering for both **1** and **2**, identified by the higher intensities of the Bragg reflections.

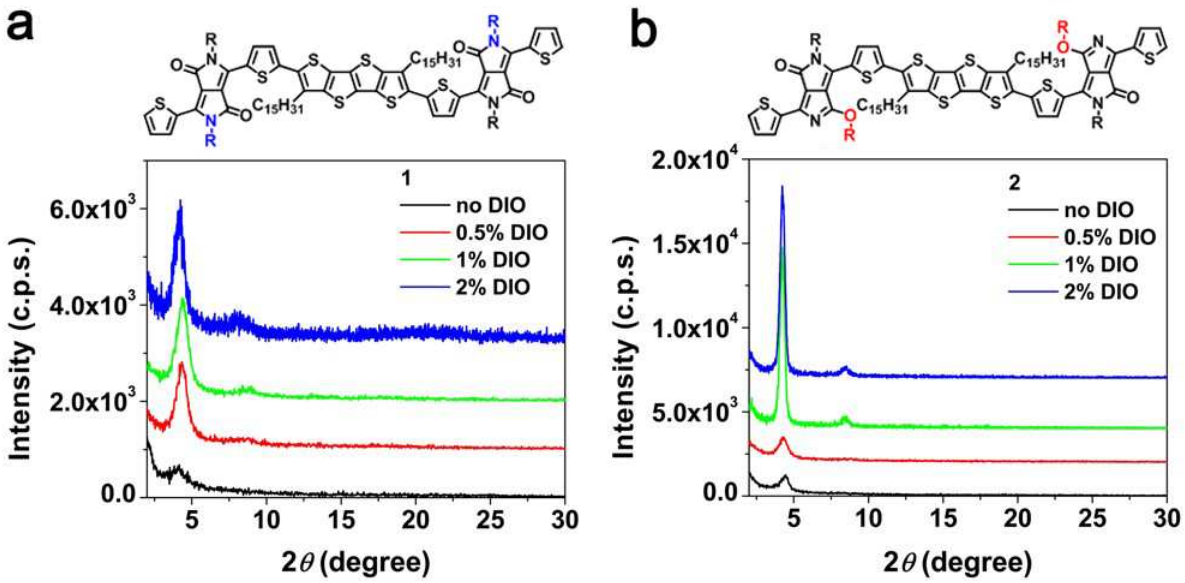

Figure 5. GIXRD patterns of **1** and **2** films prepared in CF with different *vol*% of DIO as the processing solvents. a) semiconductor **1**; b) semiconductor **2**.

Because of the promising **1** and **2** HOMO and LUMO energetics and favorable OTFT charge transport properties, OSCs were next fabricated using $PC_{71}BM$ as the acceptor with an inverted cell architecture: ITO/ZnO/active layer/MoO_3/Ag (Figure 6, with data in Table 3). Furthermore, based on the GIXRD results, DIO was used to optimize the BHJ blend film morphology for OSC performance. For blends based on **1**, a modest PCE of 0.59% is obtained for films processed without DIO. This result agrees well with the poor morphology identified by TEM and PL measurements (see details below and Figure S3). With increasing amounts of DIO loading, the PCE gradually increases to 4.02% at 1.0 vol% DIO, mainly due to a significant increase in J_{sc}. This behavior can also be readily understood by the enhanced crystallinity of **1**, benefiting from the appropriate domain size for exciton separation and efficient charge transport (see more below). However, higher DIO loadings result in decreased PCE metrics (Table S1), suggesting that ideal small molecule crystallinity is obtained using ~1.0 vol% DIO as

the processing additive. Interestingly, **2** films without DIO show even poorer OSC performance than to **1** (Figure S2,

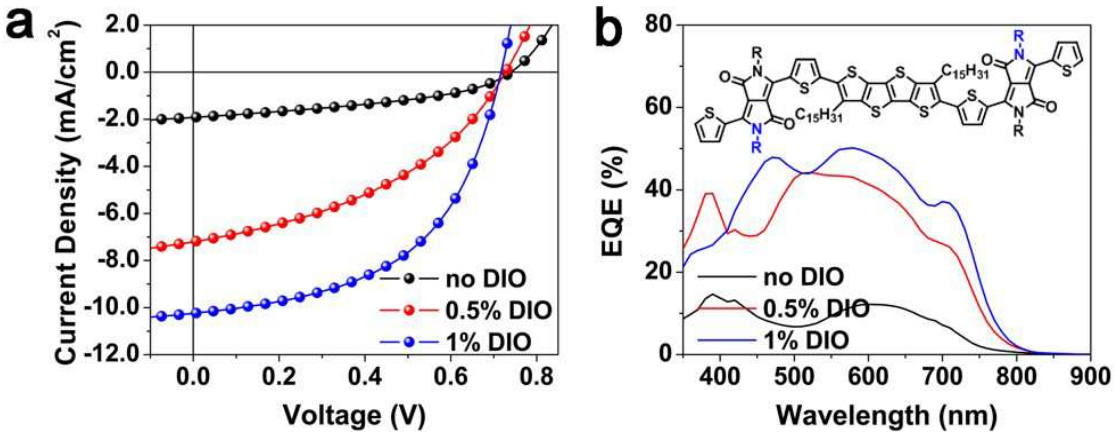

Figure 6. Inverted OSC device performance: (a) illuminated *J–V* characteristics of **1**:$PC_{71}BM$ (1:1) with varying DIO vol%. (b) External quantum efficiency (EQE) spectra of best-performing OSCs.

Tables 3 and S1). Similar to the trends observed for **1**, the addition of DIO up to 0.5-1.0 vol% gradually increases the PCE from 0.36% to 0.48%, which is mainly attributed to higher FFs. However, a slightly lower J_{sc} is also observed. The device parameters achieved using these and several other fabrication variants are summarized in Table S1. Noticeably, all OPVs based on 2 show lower V_{oc} than blends based on 1, consistent with their HOMO energies. (Figure 2)

Table 3. Summary of organic solar cell performance metrics

Semiconductor	DIO *vol*%	V_{oc} (V)	J_{sc} (mA/cm^2)	FF (%)	PCE (%) (average PCE)[a]
	0	0.745	1.93	40.9	0.59 (0.49)
1	0.5	0.732	7.25	40.1	2.13 (2.05)
	1.0	0.722	10.4	53.5	4.02 (3.98)
	0	0.520	2.13	32.7	0.36 (0.34)
2	0.5	0.597	1.67	48.2	0.48 (0.42)
	1.0	0.597	1.58	51.4	0.48 (0.43)

[a]Average PCE obtained from at least eight devices.

To investigate the efficiency of photoinduced charge transfer in the OSC active layer, photoluminescence (PL) measurements were first performed on neat **1** and **2** films, as well as their small molecule:$PC_{71}BM$ blends prepared using several different solvents (Figure S3). Interestingly, the neat films exhibit a strong PL signal for **1**, but no detectable PL for **2**. This indicates that **2** undergoes radiationless energy transfer processes responsible for energy loss after photon absorption. In principle, PL quenching can be used to qualitatively diagnose the active layer morphology of the films made with fullerene derivatives, with a higher PL quenching efficiency suggesting more intimate D-A mixing and smaller domain sizes.[4] Indeed, the blend films based on **1**:$PC_{71}BM$ processed without DIO exhibit more intense PL intensity signals versus the neat **1** films, indicating a suboptimal morphology where domain sizes may be larger than the typical exciton diffusion lengths of 5-20 nm. However, with 0.5 vol% and 1.0

vol% DIO as the processing additive, the PL quenching efficiencies are significantly increased, suggesting an improved morphology for exciton dissociation.

Grazing incidence wide angle X-ray scattering (GIWAXS) spectra were next acquired to examine the microstructural details of the OSC active layers. The neat films of both **1** and **2** exhibit similar GIWAXS patterns, with a single lamellar Bragg feature (Figures 7a, d). The paucity of reflections indicates similar d-spacings and domain sizes for **1** and **2** films. However, upon the addition of $PC_{71}BM$, the ordering of the small molecules in these blends diverges substantially for **1** and **2**, resulting in drastically different film morphologies. In the case of **1**-based films, the lamellar reflection is retained upon $PC_{71}BM$ addition (Figures 7b, g), and when the blend film is processed with 1 vol% DIO it develops significantly more crystallinity, exhibiting both n = 2 and n = 3 order reflections for the lamellar stacking (Figure 7c, g). In contrast, semiconductor **2** appears to lose all order upon blending with $PC_{71}BM$ (Figure 7e, h). When processed with DIO, a single lamellar Bragg peak does appear, but not the n = 2 and n = 3 order reflections (Figures 7f, h). Additionally, the DIO-processed blend films of **2** exhibit a reduced intensity for the $PC_{71}BM$ reflection, likely attributable to extensive interpenetration of **2** and $PC_{71}BM$, suggestive of creating blend films with a predominantly mixed phase.

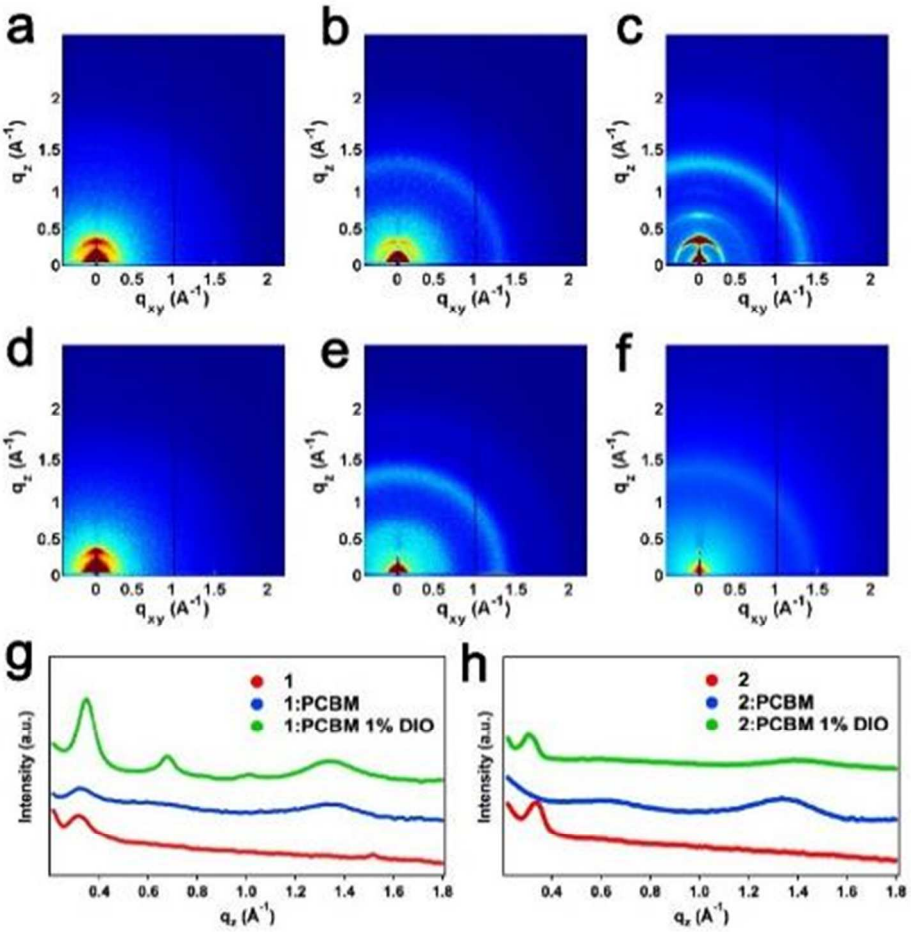

Figure 7. Two-dimensional (2D) grazing incidence wide-angle X-ray scattering (GIWAXS) images of **1** and **2**: a, d) neat film processed with CF; b, e) in blend film with $PC_{71}BM$ (1:1 w/w) processed with CF; c, f) in blend film processed with CF:DIO = 99%:1%, v/v. g, h) out-of-plane linecuts of 2D GIWAXS for **1** and **2**, respectively.

Transmission electron microscopy (TEM) images and AFM surface tomography images for blend films with $PC_{71}BM$ are shown in Figure 8. Without DIO, **1**:$PC_{71}BM$ film evidence relatively large-scale

phase separation on the order of 20-50 nm, which likely indicates a limited interface between **1** and $PC_{71}BM$. However, when 0.5 vol% DIO is added, the blend film morphology changes, revealing semicrystalline nanofibrillar structures that are well-blended with $PC_{71}BM$. Further addition of DIO up to 1 vol% induces higher crystallinity in the **1**-based films, which is consistent with the enhanced J_{sc} metrics. In marked contrast, the TEM images of the **2**:$PC_{71}BM$ films do not exhibit significant electron density contrast nor obvious ordering, implying the absence of discrete small molecule and $PC_{71}BM$ domains,

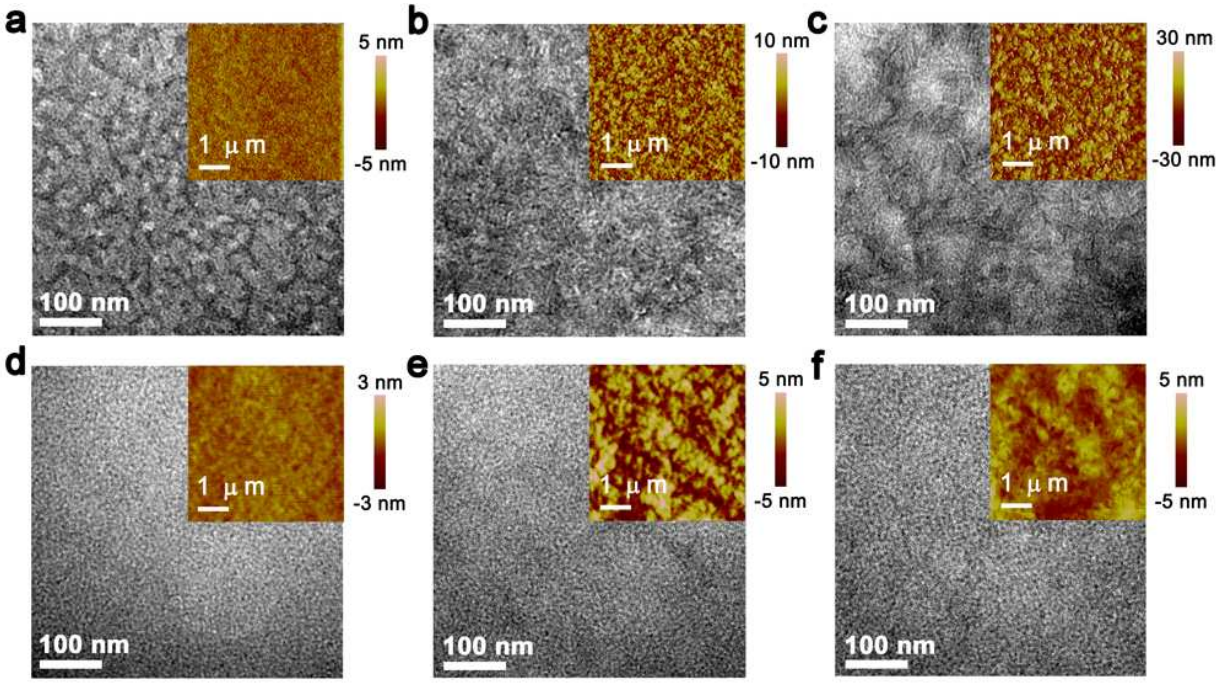

Figure 8. TEM and tapping-mode AFM (inset) images for blend films used for OSC fabrication. a, b, c) **1**:$PC_{71}BM$ = 1:1, processed in CF, CF:DIO (99.5%:0.5%, v/v) and CF:DIO(99%:1%, v/v) as processing solvents, respectively. d, e, f) **2**:$PC_{71}BM$ = 1:1, processed in CF, CF:DIO (99.5%:0.5%, v/v) and CF:DIO(99%:1%, v/v) as processing solvents, respectively. TEM scan area: 0.5 μm × 0.5 μm. AFM scan area: 5 μm × 5 μm. CF = $CHCl_3$.

but rather intimate D + A mixing. In terms of OSC performance, this microstructure is likely to increase both geminate and non-geminate recombination losses.[27] This result also agrees well with the GIWAXS measurements, where the bulk-heterojunction mixture of small molecule **2**:$PC_{71}BM$ shows predominantly miscible, amorphous characteristics.

To investigate the charge transport characteristics more closely related to the photodiode, space charge limited current (SCLC) measurements were performed on the neat semiconductor films, as well as on the blend films processed with various DIO loadings (Figure 9 and Table S2). In the hole-only diodes, the current density (J) as a function of applied electric field (E) in the space charge limited regime is given by eq. 1, where by fitting the J-E curve it is possible to extract the zero-field mobility, μ_0.[48] Here γ is a field-dependent coefficient, while ε_s and L are the semiconductor permittivity (taken as $3\varepsilon_0$) and thickness, respectively.

$$J = \frac{9}{8}\frac{\epsilon_s}{L}E^2\mu_0\exp\left(\gamma\sqrt{E}\right) \quad (1)$$

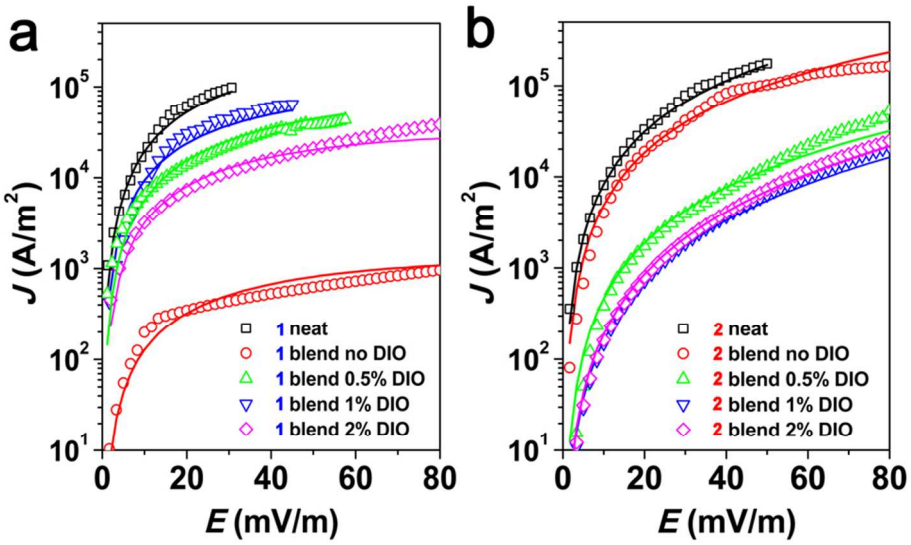

Figure 9. Typical current density-electric field semilogarithmic plots for hole-only devices for neat **1** and **2** films, and their blend films with $PC_{71}BM$ (50:50 wt%). Measured data are shown as symbols, while solid lines are best fits to the space charge limited conduction (SCLC) model. Mobilities are extracted from the fitting.

Single diode hole-only and electron-only devices were fabricated using MoO_3/Au contacts. For neat **1** and **2** films, the SCLC mobilities are as high as 2.5×10^{-2} $cm^2V^{-1}s^{-1}$ and 4.9×10^{-3} $cm^2V^{-1}s^{-1}$, respectively. These SCLC motilities are comparable to those achieved in optimized OTFTs, corroborating the excellent, nearly omnidirectional charge transport characteristics of both materials. For the blend films with $PC_{71}BM$ added, the SCLC mobilities for **1** and **2** fall to 1.6×10^{-4} $cm^2V^{-1}s^{-1}$, and 2.3×10^{-3} $cm^2V^{-1}s^{-1}$,

respectively. Note that the addition of DIO in the processing solvent introduces opposite trends in SCLC mobilities for the BHJ films of **1** and **2**. Specifically, DIO greatly increases the SCLC mobility for **1**:$PC_{71}BM$ blend films up to $\mu_h = 1.1\times10^{-2}$ $cm^2V^{-1}s^{-1}$ with 1.0 vol% DIO, which is only slightly less than that observed for the neat film of **1**. This indicates that the greater crystallinity induced by DIO can promote vertical percolative pathways for blend films of **1**. This result is in excellent agreement with the increased OPV FFs for blend films of **1** processed with DIO. However, we also note that further FF enhancements may be precluded by limited carrier lifetimes, as a result of currently suboptimal morphology.[4] Interestingly, DIO negatively influences the SCLC mobilities for **2**:$PC_{71}BM$ blend films, with μ_h as low as $5.0 \pm 0.1 \times 10^{-5}$ $cm^2V^{-1}s^{-1}$ measured upon using 1.0 vol% DIO. Such a steep reduction in mobility is consistent with the reduced J_{sc} metrics and poor blend film morphologies observed by the GIWAXS and TEM measurements discussed above.

Conclusions

In this study two novel **DPP**-based small molecules employing a central electron-rich fused tetrathienoacene (**TTA)** core, **DDPP-TTAR** and **DDPP'-TTAR**, were designed, synthesized, and characterized. The expansive **TTA** cores provide excellent molecular coplanarity and close π-stacking, thus enhancing intermolecular interactions and affording favorable macroscopic morphologies for charge transport. Benefitting from the electron-deficiency of the **DPP** cores, both materials have small optical band gaps and suitable HOMO energies for hole injection in OTFTs. These properties yield sizable OTFT mobilities in the range 0.02-0.09 $cm^2V^{-1}s^{-1}$. Furthermore, XRD and GIWAXS measurements indicate that the spin-coated thin film morphologies of both molecules are strongly susceptible to the use of DIO as a solvent additive. Specifically, small quantities of DIO of up to 1 vol% significantly enhance the crystallinity of **DDPP-TTAR** films. When incorporated into inverted OSC active layers, good PCEs of 4.0% are achieved, which are among the highest yet reported for fused thiophene based small molecules. These results indicate the **TTA** cores are promising donor moieties for OTFT and OSC materials

development. However, the **DDPP'-TTAR** isomer, despite good OTFT mobility, is found to predominantly form miscible mixtures with $PC_{71}BM$, thus resulting in relatively poor phase separation morphologies, hence poor PCEs. This study of structure-property relationships in **TTA**-based small molecules identifies the importance of fine-tuning the molecular stacking and thin film morphologies by selecting compatible D-A moieties and processing solvents – a key ingredient for achieving high performance OTFTs and OSCs.

Acknowledgements

This research was supported as part of the ANSER Center, an Energy Frontier Research Center funded by the U.S. Department of Energy, Office of Science, and Office of Basic Energy Sciences under Award Number DE-SC0001059, by AFOSR (FA9550-08-1-0331), and by Polyera Corp. We thank the NSF-MRSEC program, through the Northwestern University Materials Research Science and Engineering Center, for characterization facilities (DMR-1121262), and the Institute for Sustainability and Energy at Northwestern (ISEN), for partial equipment funding. Financial assistance for this research was also provided by the National Science Council, Taiwan, Republic of China (Grant Numbers NSC102-2113-M-008-004 and NSC102-2923-M-008-004-MY2)

Notes and references

[a] Department of Materials Science and Engineering and Argonne Northwestern Solar Energy Research Center (ANSER), Northwestern University, 2145, Sheridan Road, Evanston, Illinois, 60208 (USA).

[b] Department of Chemistry, National Central University, Chung-Li, Taiwan, ROC.

[c] Department of Chemistry and the Materials Research Center, the Argonne-Northwestern Solar Energy Research Center, Northwestern University, 2145 Sheridan Road, Evanston, Illinois, 60208, USA.

[d] Polyera Corporation, 8045 Lamon Avenue, Skokie, Illinois 60077, USA.

‡ N. Zhou and S. Vegiraju contributed equally to this work.

Electronic Supplementary Information (ESI) available: [details of any supplementary information available should be included here]. See DOI: 10.1039/b000000x/

References

1. C. M. Proctor, C. Kim, D. Neher and T.-Q. Nguyen, *Adv. Funct. Mater.*, 2013, 23, 3584-3594.
2. B. Walker, A. B. Tamayo, X.-D. Dang, P. Zalar, J. H. Seo, A. Garcia, M. Tantiwiwat and T.-Q. Nguyen, *Adv. Funct. Mater.*, 2009, 19, 3063-3069.
3. Y. Liu, X. Wan, F. Wang, J. Zhou, G. Long, J. Tian and Y. Chen, *Adv. Mater.*, 2011, 23, 5387-5391.
4. X. Guo, N. Zhou, S. J. Lou, J. Smith, D. B. Tice, J. W. Hennek, R. P. Ortiz, J. T. L. Navarrete, S. Li, J. Strzalka, L. X. Chen, R. P. H. Chang, A. Facchetti and T. J. Marks, *Nat Photon*, 2013, 7, 825-833.
5. H. Yan, Z. Chen, Y. Zheng, C. Newman, J. R. Quinn, F. Dotz, M. Kastler and A. Facchetti, *Nature*, 2009, 457, 679-686.
6. D. Fernandez, A. Viterisi, J. W. Ryan, F. Gispert-Guirado, S. Vidal, S. Filippone, N. Martin and E. Palomares, *Nanoscale*, 2014, 6, 5871-5878.
7. J. Liu, B. Walker, A. Tamayo, Y. Zhang and T.-Q. Nguyen, *Adv. Funct. Mater.*, 2013, 23, 47-56.
8. E. Ripaud, D. Demeter, T. Rousseau, E. Boucard-Cétol, M. Allain, R. Po, P. Leriche and J. Roncali, *Dyes and Pigments*, 2012, 95, 126-133.
9. Y. Qiao, Y. Guo, C. Yu, F. Zhang, W. Xu, Y. Liu and D. Zhu, *J. Am. Chem. Soc.*, 2012, 134, 4084-4087.
10. S.-L. Suraru, U. Zschieschang, H. Klauk and F. Wurthner, *Chem. Commun.*, 2011, 47, 1767-1769.
11. A. B. Tamayo, B. Walker and T.-Q. Nguyen*, *J. Phys. Chem. C*, 2008, 112, 11545-11551.
12. M. Tantiwiwat, A. Tamayo, N. Luu, X.-D. Dang and T.-Q. Nguyen, *J. Phys. Chem. C*, 2008, 112, 17402-17407.
13. Y. Lin, P. Cheng, Y. Li and X. Zhan, *Chemical Communications*, 2012, 48, 4773-4775.
14. Y. Lin, L. Ma, Y. Li, Y. Liu, D. Zhu and X. Zhan, *Advanced Energy Materials*, 2013, 3, 1166-1170.
15. H. Bai, P. Cheng, Y. Wang, L. Ma, Y. Li, D. Zhu and X. Zhan, *Journal of Materials Chemistry A*, 2014, 2, 778-784.
16. Y. Li, P. Sonar, L. Murphy and W. Hong, *Energy Environ. Sci.*, 2013, 6, 1684-1710.
17. I. Kang, H.-J. Yun, D. S. Chung, S.-K. Kwon and Y.-H. Kim, *Journal of the American Chemical Society*, 2013, 135, 14896-14899.

18. J. Y. Back, H. Yu, I. Song, I. Kang, H. Ahn, T. J. Shin, S.-K. Kwon, J. H. Oh and Y.-H. Kim, *Chemistry of Materials*, 2015, 27, 1732-1739.
19. J. Li, Y. Zhao, H. S. Tan, Y. Guo, C.-A. Di, G. Yu, Y. Liu, M. Lin, S. H. Lim, Y. Zhou, H. Su and B. S. Ong, *Sci. Rep.*, 2012, 2.
20. J. W. Jung, F. Liu, T. P. Russell and W. H. Jo, *Energy Environ. Sci.*, 2012, 5, 6857-6861.
21. H. Choi, S.-J. Ko, T. Kim, P.-O. Morin, B. Walker, B. H. Lee, M. Leclerc, J. Y. Kim and A. J. Heeger, *Advanced Materials*, 2015, 27, 3318-3324.
22. Y. Sun, G. C. Welch, W. L. Leong, C. J. Takacs, G. C. Bazan and A. J. Heeger, *Nat Mater*, 2012, 11, 44-48.
23. T. S. van der Poll, J. A. Love, T.-Q. Nguyen and G. C. Bazan, *Adv. Mater.*, 2012, 24, 3646-3649.
24. A. K. Kyaw, D. H. Wang, V. Gupta, J. Zhang, S. Chand, G. C. Bazan and A. J. Heeger, *Adv. Mater.*, 2013, 25, 2397-2402.
25. L. Fu, W. Fu, P. Cheng, Z. Xie, C. Fan, M. Shi, J. Ling, J. Hou, X. Zhan and H. Chen, *J. Mater. Chem. A*, 2014, 2, 6589-6597.
26. M. T. Lloyd, J. E. Anthony and G. G. Malliaras, *Mater. Today*, 2007, 10, 34-41.
27. S. R. Cowan, N. Banerji, W. L. Leong and A. J. Heeger, *Adv. Funct. Mater.*, 2012, 22, 1116-1128.
28. S. Loser, C. J. Bruns, H. Miyauchi, R. P. Ortiz, A. Facchetti, S. I. Stupp and T. J. Marks, *J. Am. Chem. Soc.*, 2011, 133, 8142-8145.
29. P.-L. T. Boudreault, J. W. Hennek, S. Loser, R. P. Ortiz, B. J. Eckstein, A. Facchetti and T. J. Marks, *Chem. Mater.*, 2012, 24, 2929-2942.
30. J. Huang, C. Zhan, X. Zhang, Y. Zhao, Z. Lu, H. Jia, B. Jiang, J. Ye, S. Zhang, A. Tang, Y. Liu, Q. Pei and J. Yao, *ACS Appl. Mater. Inter.*, 2013, 5, 2033-2039.
31. J. Youn, M.-C. Chen, Y.-j. Liang, H. Huang, R. P. Ortiz, C. Kim, C. Stern, T.-S. Hu, L.-H. Chen, J.-Y. Yan, A. Facchetti and T. J. Marks, *Chem. Mater.*, 2010, 22, 5031-5041.
32. S.-S. Cheng, P.-Y. Huang, M. Ramesh, H.-C. Chang, L.-M. Chen, C.-M. Yeh, C.-L. Fung, M.-C. Wu, C.-C. Liu, C. Kim, H.-C. Lin, M.-C. Chen and C.-W. Chu, *Adv. Funct. Mater.*, 2014, 24, 2057-2063.
33. J. Youn, P.-Y. Huang, S. Zhang, C.-W. Liu, S. Vegiraju, K. Prabakaran, C. Stern, C. Kim, M.-C. Chen, A. Facchetti and T. J. Marks, *Journal of Materials Chemistry C*, 2014, 2, 7599-7607.
34. H. H. Fong, V. A. Pozdin, A. Amassian, G. G. Malliaras, D.-M. Smilgies, M. He, S. Gasper, F. Zhang and M. Sorensen, *J. Am. Chem. Soc.*, 2008, 130, 13202-13203.
35. J. Youn, P.-Y. Huang, Y.-W. Huang, M.-C. Chen, Y.-J. Lin, H. Huang, R. P. Ortiz, C. Stern, M.-C. Chung, C.-Y. Feng, L.-H. Chen, A. Facchetti and T. J. Marks, *Adv. Funct. Mater.*, 2012, 22, 48-60.
36. Y. S. Yang, T. Yasuda, H. Kakizoe, H. Mieno, H. Kino, Y. Tateyama and C. Adachi, *Chem. Commun.*, 2013, 49, 6483-6485.
37. M.-C. Chen, Y.-J. Chiang, C. Kim, Y.-J. Guo, S.-Y. Chen, Y.-J. Liang, Y.-W. Huang, T.-S. Hu, G.-H. Lee, A. Facchetti and T. J. Marks, *Chem. Commun.*, 2009, 1846-1848.
38. Y. M. Sun, Y. Q. Ma, Y. Q. Liu, Y. Y. Lin, Z. Y. Wang, Y. Wang, C. A. Di, K. Xiao, X. M. Chen, W. F. Qiu, B. Zhang, G. Yu, W. P. Hu and D. B. Zhu, *Adv. Funct. Mater.*, 2006, 16, 426-432.
39. M.-C. Chen, S. Vegiraju, C.-M. Huang, P.-Y. Huang, K. Prabakaran, S. L. Yau, W.-C. Chen, W.-T. Peng, I. Chao, C. Kim and Y.-T. Tao, *Journal of Materials Chemistry C*, 2014, 2, 8892-8902.
40. C. Lu and W.-C. Chen, *Chem. Asian J.*, 2013, 8, 2813-2821.
41. J. K. Park, C. Kim, B. Walker, T.-Q. Nguyen and J. H. Seo, *RSC Advances*, 2012, 2, 2232-2234.
42. M. He and F. Zhang, *J. Org. Chem.*, 2006, 72, 442-451.
43. G. Qian, J. Qi, J. A. Davey, J. S. Wright and Z. Y. Wang, *Chem. Mater.*, 2012, 24, 2364-2372.
44. W. L. Kalb, T. Mathis, S. Haas, A. F. Stassen and B. Batlogg, *Appl. Phys. Lett.*, 2007, 90, -.

45. J. K. Lee, W. L. Ma, C. J. Brabec, J. Yuen, J. S. Moon, J. Y. Kim, K. Lee, G. C. Bazan and A. J. Heeger, *J. Am. Chem. Soc.*, 2008, 130, 3619-3623.
46. Y. Huang, W. Wen, S. Mukherjee, H. Ade, E. J. Kramer and G. C. Bazan, *Adv. Mater.*, 2014, 26, 4168-4172.
47. A. K. K. Kyaw, D. H. Wang, C. Luo, Y. Cao, T. Q. Nguyen, G. C. Bazan and A. J. Heeger, *Adv Energy Mater*, 2014, 4, 1301469.
48. D. F. Barbe, *J. Phys. D: Appl. Phys.*, 1971, 4, 1812.